

Effects of particle size and oxide shell on variable stiffness performance of phase-changing materials

Journal of Composite Materials
2023, Vol. 57(4) 619–631
© The Author(s) 2022
Article reuse guidelines:
sagepub.com/journals-permissions
DOI: 10.1177/00219983221129252
journals.sagepub.com/home/jcm


Trevor L Buckner¹ , Zachary J Farrell², Amir M Nasab¹ and Rebecca Kramer-Bottiglio¹

Abstract

Phase-changing materials have recently found use as particulate fillers to engender stiffness-changing behavior in composites. In the transition from solid to liquid particles, the composite modulus can be significantly reduced, and then raised again as the particles are allowed to solidify. While the general effect of stiffness tuning in phase-changing composites has been demonstrated in a range of studies and applications, the most drastic stiffness ranges are provided by fusible metallic alloys, which are commonly subject to the formation of oxide shells on their surfaces. In this work, we examine the effect these oxide surfaces have on variable-stiffness performance, and investigate the corresponding role of particle size. In particular, we study particles of a low-melting-point metallic alloy, Field's Metal, and we also present a facile method of manufacture that allows for control of particle size. We then manufacture a set of stiffness-changing composites using these particles and characterize mechanical performance, with the aim of controlling particle size to increase the total stiffness ratio while resisting material failure.

Keywords

Multifunctional composites, phase-change, soft robotics, variable-stiffness

Introduction

Phase-changing materials provide a unique set of properties that are made possible primarily via the reversible transition from solid to liquid (or liquid to gas) and back. Typically derived from specialized metallic alloys, waxes, or thermoplastic polymers, solid-to-liquid phase-changing materials are often used in manufacturing processes where internal shape must be temporarily held and then easily extracted via melting. For example, a pattern for investment casting must remain solid during creation of a mold, but later is melted out to leave behind the cavity for the product material.^{1,2}

More recently, a range of different phase-changing materials have become key tools for the development of mechanisms that utilize variable-stiffness or shape-change^{3–8} particularly in the field of soft robotics, where on-demand activation and suppression of rigid support structures is highly sought after.⁹ In recent years, this strategy has brought about a series of advancements toward the development of phase-changing composites – materials that have gained some added functionality via the inclusion of an additive with phase-changing properties. In particular, soft materials such as elastomers, when modified via wax or fusible alloy micro-particle fillers, benefit from substantial increases in rigidity in

room-temperature environments, yet retain access to the flexibility inherent in the matrix material via reversible heating and melting of the internal phase-changing additive.^{10–12}

While the general effect of stiffness tuning in phase-changing composites has been demonstrated in a range of studies and applications, the most drastic stiffness ranges are provided by fusible metallic alloys, which are commonly subject to the formation of oxide shells on their surfaces. This oxide layer, often orders of magnitude more rigid than the underlying material, has a pronounced, detrimental effect on the stiffness-changing performance of a given composite. Motivated by this observation, we note that controlling for particle size can offset this issue and as such

¹School of Engineering and Applied Science, Yale University, New Haven, CT, USA

²US Air Force Research Laboratory, Dayton, OH, USA

Corresponding author:

Rebecca Kramer-Bottiglio, School of Engineering and Applied Science, Yale University, New Haven, CT 06520, USA.

Email: rebecca.kramer@yale.edu.

Correction (February 2023): Article updated with equation 8 and Figure 5 since its original publication.

is a key design parameter for maximizing variable-stiffness performance, although this brings with it other tradeoffs in material properties.

Theoretical efforts applying Mori-Tanaka and Eschelby equivalent inclusion theory can aid in the selection of composite filler dimensions to determine or design the mechanical properties of standard composite materials with isotropic particles.^{13–15} However, few theoretical studies have been able to capture the variation in mechanical properties of composites that result from phase-changing particles,¹⁶ particularly in combination with a persistent oxide shell. Further, most previous studies of this nature have considered a low packing fraction of particles, $\phi < 0.2$, whereas recent variable-stiffness composites using fusible metallic alloys^{10,12,17–19} often utilize higher concentrations, $0.3 \leq \phi \leq 0.5$, where there are strong interactions between particles. This study aims to fill these gaps in knowledge via the use of other modern core-shell modelling techniques, backed by experimental measurements.

In this work, we examine composites made from particles of Field's metal (FM), a metallic alloy known for its exceptionally low melting point ($\sim 62^\circ\text{C}$) and non-hazardous composition. Generally, a variable-modulus composite should be strong and fracture resistant, in addition to maximizing its modulus range. Therefore, our study characterizes the impacts of particle size and oxide formation on each of these dependent properties within the unique requirement space of variable-stiffness composites. We developed a manufacturing method that allows for tight control of particle size with high sphericity, in addition to a facile method of modifying the surface structure of FM particles to improve mechanical bonding.

Materials and methods

Particle manufacture

Field's metal particles are manufactured via a process improved from Buckner et al¹⁹ by modifying the thixotropic (shear-thinning) mixing techniques from Yup et al²⁰ and Eristoff et al.²¹ A 1000-mL beaker is filled with 200 mL of a thixotropic aqueous mixture, in this case a solution of deionized water and a confectionery sodium alginate powder (Modernist Pantry) with a loading of 2 wt%. This mixture nominally has a viscosity of ~ 2.6 pa·s (similar to room-temperature honey), but thins to ~ 0.2 pa·s (similar to maple syrup) when subjected to a shear rate of 1000/s.²¹ The mixture is then warmed to approximately 70°C by placing the beaker inside of a heated silicone oil bath (95°C). Ingots of Field's metal (Roto144 F, RotoMetals, Inc.) with a total weight of 60 g are placed inside the heated medium and allowed to melt over the course of about 10 min. Once fully melted, the Field's metal is broken apart using a homogenizer (Cole-Parmer LabGEN 850) with a 20 mm diameter saw-tooth generator attachment for 60 s,

during which time the thixotropic mixture flows freely. After homogenization is stopped, the medium vitrifies in place almost immediately, capturing the Field's metal droplets in suspension where they are allowed to cool and solidify over time with minimal aggregation or settling. The mixture can be diluted in a large container by stirring in additional water, at which point the FM particles are able to settle and collect at the bottom of the container. The supernatant can be decanted off, and the FM particles are extracted and rinsed, and allowed to fully dry in a vacuum chamber overnight (Figure 1(a)). Multiple diluting-decating steps may be required for smaller particles, which will not fully settle until a majority of the sodium alginate mixture has been removed. Because the particles become fully solid during the cooling step, they can be handled directly without the need of any additional stabilizers or encapsulants that might be needed for liquid-core droplets.²² Further, in contrast to Yup et al,²⁰ this method does not require any additional solvent or enzyme to release the particles from the medium as it does not form a polymerized gel. Indeed, with sodium alginate powder and water as the only required components, this process also carries the benefit of being inexpensive, simple to execute, and eco-friendly with sustainable by-products.

Particle size control

FM particle size is controlled by adjusting the homogenizer mixing speed. At higher mixing velocities, the FM is broken into smaller droplets (Figure 1(b)). Compared to previously-reported methods,¹⁹ this technique tends to generate a more predictable and less polydisperse spread of particle sizes (Figure 1(c)), which in turn results in a higher yield as large unusable particles are not generated. Further, the high counts of nanoscale shards broken off from fractured particles found in previous works¹⁹ do not appear to be present after microscope inspection (Figure 1(d)), resulting in more consistent and predictable material behaviors.

Particle surface texturing

As the vitrified thixotropic mixture inhibits aggregation and settling of molten FM droplets, it also dampens the residual shear from the homogenizing process and negates much of the deformation that would occur due to gravity. Suspended in this medium, the absence of external forces allows the surface tension to dominate and pull the droplets into spheres, while the gradual cooling of the mixture allows the particles to solidify approximately uniformly. All of this contributes to particles that are not only highly spherical, but also possess a very smooth surface.²⁰ The surface texture can be roughened as an additional processing step to improve bonding between the particles and the host matrix material. After the particles have been collected and dried, they are heated to approximately 80°C , thereby melting the

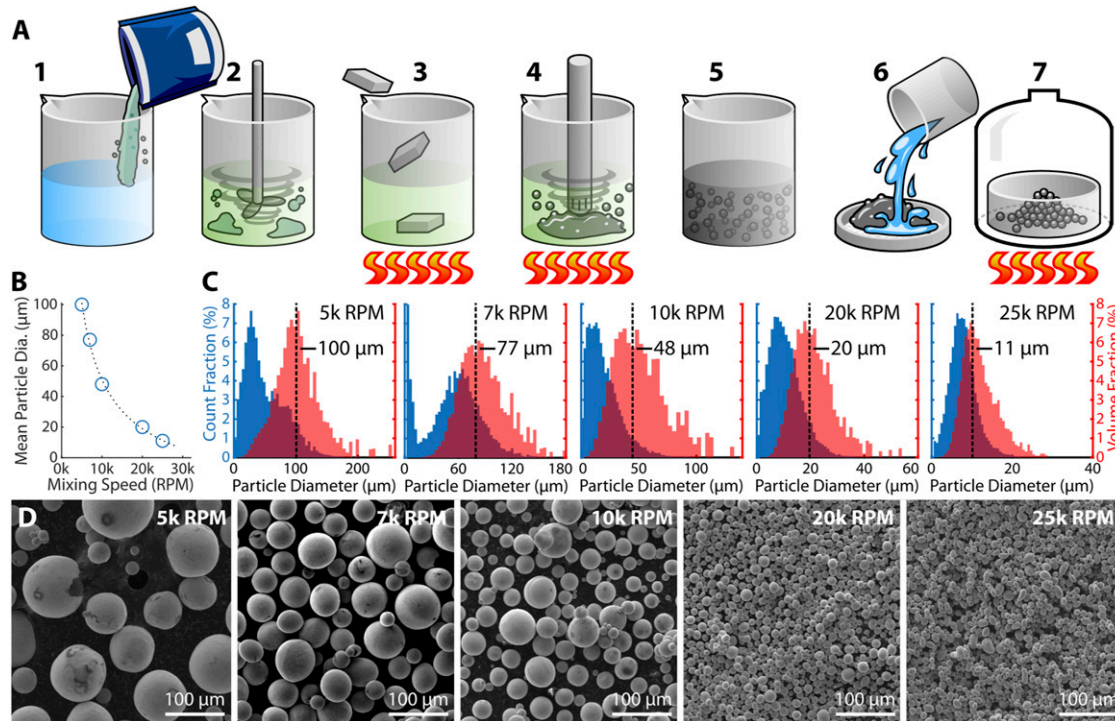


Figure 1. Manufacture and characterization of FM particles. (a) FM particle manufacturing process: (1) Sodium alginate is added into deionized water and (2) mixed until homogenous. (3) FM ingots are added and heated. (4) Molten metal is homogenized at the desired mixing rates. (5) Particles cool and solidify. (6) Alginate is rinsed from FM particles. (7) Particles are dried in a vacuum oven. (b) Mean particle diameter dependent on homogenization speed. (c) Particle size distribution (by count, blue; by volume, red). (d) Scanning Electron Microscopy (SEM) images for each size, taken at the same scale.

FM particle cores while the oxide shell remains intact. At this point, the particles are immediately submerged in an ice bath, which causes the particles to shrivel slightly, resulting in a wrinkled surface texture.

Results

Effects of particle size

Matrix-inclusion bonding. The quality of bonding between the host matrix and the particle inclusions is key to achieving several desirable properties in a variable-stiffness composite. Generally, secure bonding corresponds to higher material strength,¹⁵ and poor bonding has been shown to cause early fracture in previous examples of FM composites.²³ While there exist many methods to achieve high bonding in Field's metal or other core-shell particles, including chemical, heat, and mechanical treatments,²⁴ they often disrupt the eutectic balance of the alloy or increase oxide growth which inhibits the stiffness change performance. As such, this section remains strictly focused on mechanical bonding strength due to particle size, which will be applicable to variable stiffness fillers regardless of material.

In an earlier work, we noted that a debonding event can be detected by monitoring the flexural modulus of the composite as it is stretched. As the rigid particles embedded within an elastomeric matrix begin to detach from the matrix material, they no longer contribute to the material stiffness, which will manifest as a sudden drop in elastic modulus at a certain level of strain.¹⁰ We used this observable drop in modulus as a measure of the onset of debonding, by which we qualitatively compared the bonding effectiveness of FM fillers dependent on particle diameter. The test was performed by axially stretching composite specimens of each particle inclusion size (5 of each) at a loading of 30 vol%, using Dragon Skin 10 Medium (Smooth-On) as the elastomeric matrix material. Specimens were cut out from a film of cured FM-Dragon Skin, resulting in rectangular coupons (100 mm × 8 mm × 0.6 mm). Fabric reinforcement tabs (20 mm × 8 mm) were adhered to the front and back at both ends of each specimen, providing an inextensible region for secure gripping in the testing clamps, and resulting in a stretchable region of 60 mm × 8 mm. Specimens were loaded at rate of 120 mm/min. We mark the debonding event for each specimen as the point of tightest curvature at the “elbow” of the resulting stress-strain curves (Figure 2(A)). The results show that particles of smaller diameter are able to maintain the bond at increased levels of stress and strain

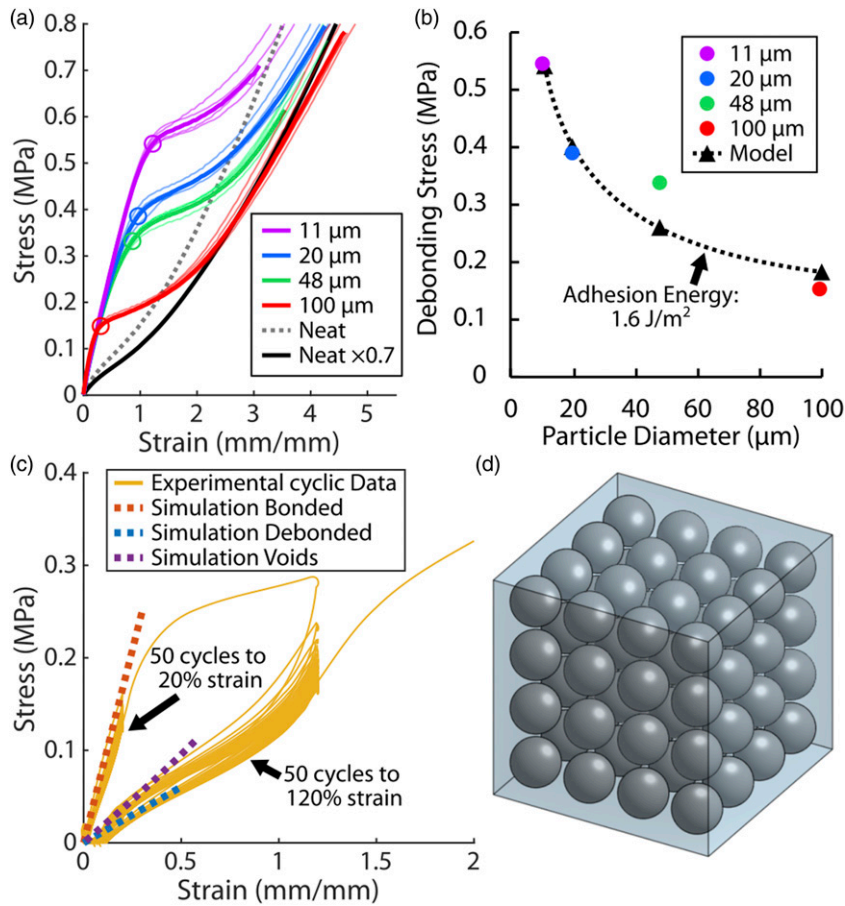


Figure 2. Particle size versus particle-matrix bonding strength. (a) Dragon Skin-FM specimens strained beyond the filler debonding point, marked with a circle. Includes neat Dragon Skin, at full scale as well as scaled to 70% stress to approximate 30% void content. (b) Mean debonding stress as a function of particle diameter, and expected debonding stress from model given a particle/matrix surface adhesion energy of 1.6 J/m^2 . (c) Cyclic strain data for a specimen with 30 vol% of $100 \mu\text{m}$ particles, compared with FEA simulation data. (d) Simulated cube (30 vol%, $105 \mu\text{m}$ diameter particles).

(Figure 2(B)), which we attribute to the larger total surface area involved at the material interfaces that consequently increases the total energy absorbed per volume before debonding occurs.²⁵ These results indicate that in the absence of chemical binders or adhesives, the use of smaller particles can contribute to a tougher variable-stiffness composite.

Strain cycling the material several times to 20% strain, a safe level below the debonding point, results in a largely repeatable stress-strain curve. However, once the debonding event has occurred, the damage appears to remain in subsequent strain cycles (Figure 2(C)). Re-heating the specimen to melt the particles is not sufficient to restore the matrix-filler bonding, likely due to the presence of the thin oxide shell on the particle surface. Instead, it is necessary to heat and then apply a large amount of strain to disrupt the oxide shell and allow the melted material to reflow and reform the mechanical bond onto the microtexture of the matrix.¹⁰

We confirmed that the modulus change after the “elbow” point is indeed due to debonding by modeling the behavior of bonded and non-bonded filler materials with Finite-Element Analysis (FEA, SolidWorks 2020). In these tests, we simulated a set of soft cubes filled with $105 \mu\text{m}$ solid particles at 30 vol% and subjected them to small displacements (Figure 2(D)). If the surfaces are fully bonded, the measured stresses indicate a high elastic modulus in agreement with our experimental data (Figure 2(C)). If the simulated particles are not bonded, the effective modulus closely matches experimental data for specimens that have been manually stretched beyond the debonding point before testing. Further, we note that the unbonded simulation has very similar results to an additional simulation wherein all particles are replaced by voids. That is, the addition of filler particle material that fails to bond to the matrix will behave similarly to voids and in-fact reduce the composite modulus to below that of the neat matrix material. Further, if bonding is poor, reducing

particle size will also increase crack propagation since existing cracks do not have to deviate as far from particle to particle to continue spreading.²⁶ The Dragon Skin 10 matrix material was modeled using the Ogden model parameters: $\alpha_1=1.62$, $\alpha_2=5.18$, $\alpha_3=-13.42$, $\mu_1=80,031.09$ Pa, $\mu_2=1049.90$ Pa, $\mu_3=32.89$ Pa,²⁷ and the Field's Metal particles were modeled as a linear elastic material with parameters: Poisson's ratio=0.33, elastic modulus=9.2 GPa.¹⁹

Our experimental results also closely match analytical debonding models. For an FM composite with a known particle size, the total energy absorbed up until the debonding point is measured as the area under the stress-strain curve, γ_{total} . Given a FM volume loading of $\phi = 0.3$, we know that some portion of the absorbed energy is due to stretching the Dragon Skin in the remaining 70% of the volume, γ_{silicone} . This is measured as the area under the stress-strain curve of a neat Dragon Skin 10 specimen to the same strain point, multiplied by $1 - \phi$. Note in Figure 2(A) that scaling the stress of the neat specimen to 70% causes it to follow the trajectory of the other curves. The remaining absorbed energy, γ_{debond} , is due to particle-matrix interfaces. Therefore, given the particle size and loading volume, we can calculate the total particle-matrix interfacial surface area $A_{\text{interface}}$ to determine the per-area adhesion energy γ_{surface} .

$$\begin{aligned}\gamma_{\text{debond}} &= \gamma_{\text{total}} - (1 - \phi)\gamma_{\text{neat}} \\ \gamma_{\text{surface}} &= \gamma_{\text{debond}}/A_{\text{interface}}\end{aligned}\quad (1)$$

As expected, γ_{surface} is fairly consistent across particle sizes, ranging from 1.30–1.88 J/m². Using the debonding equation provided by Lauke²⁵ and Nicholson²⁸ which assumes the particles are rigid compared to the matrix material, we can see that a surface energy of 1.6 J/m² provides predicted debonding stress points that match our experimental elbow points very closely (Figure 2(B))

$$\sigma_{\text{debond}} = \frac{1}{3(1 - \nu_m)} \sqrt{\frac{16\gamma_{\text{surface}}E_m(1 + \nu_m)}{d}}\quad (2)$$

where σ_{debond} is the predicted debonding stress, ν_m and E_m are the Poisson's ratio (0.5, estimate) and Young's modulus (186 kPa¹⁰) of the matrix material, and d is the average particle size. The 48 μm particle size does not quite follow the curve, but we attribute this to the wider particle polydispersity of those samples (Figure 1(C)) and small inconsistencies in the manual manufacturing process.

We noted in Section 2.3 that the highly smooth surface of the FM particles (Figure 3(A)) may have a negative impact on particle-matrix bonding, although this can be improved further by treating the particle surface so as to modify its texture, creating additional physical features on the surface to provide robust mechanical connection. We achieved

surface roughening by heating the particles, and then submerging them in an ice bath to induce wrinkling of the oxide shell as the particle shrivels (Figure 3(B)). After this process, the FM particles lose their highly-reflective shiny surface and appear a dull gray to the naked eye.

Using these roughened particles of the 11 μm size, we repeated the strain experiment above and compared it to the untreated particles. Figure 3(C) shows that the debonding onset strain is indeed extended by approximately 16% and the debonding stress is increased by 11%, corresponding to a predicted adhesion energy of 2.08 J/m² (Equation (2)), which is a 30% increase compared to smooth particles. At the same time, the composite elastic modulus appears to be unaffected. Further modification of the surface structure to include deeper crevices and folds can likely improve this bond, and may be achievable by a similarly facile procedure.

Composite Uniformity and Particle Settling. Depending on the cure time of the matrix material, filler particles may settle at the bottom of the composite. This naturally leads to nonhomogeneous and unpredictable material properties²⁹ due to particle agglomeration or the emergence bilayer interactions,³⁰ and so is generally undesirable. The density of FM results in obvious settling when the particles are large (>100 μm diameter). In this work, we observed the cross-section of Dragon Skin 10 with 30 vol% FM of different particle sizes. While the 100 μm particles do settle rapidly to the bottom of the composite (Figure 4(A)), specimens using smaller sizes begin to appear well-distributed (Figures 4(B)-(D)). We also note that hand-mixing of composites was significantly easier with decreasing particle size, which may have aided in the even distribution.

We further note that at 50 vol% loading, a number of voids begin to appear throughout the matrix¹⁹ which can be detrimental to the strength of a variable-stiffness composite. The presence of voids with increasing filler content is a known phenomenon.³¹ Following similar reports,^{32,33} we suspect that as the composite is mixed by hand, small pockets of air become entrapped in the resin. Although specimens undergo a vacuum process to evacuate the captured air, this appears to become less successful with increasing particle settling. Perhaps, this is because in addition to the resin already being highly viscous, particle sedimentation is known to create aggregates which further impede the flow of trapped air through the resin medium,³⁴ or cause uneven filling over the specimen height.²⁹ To measure void content, we created an additional set of composite samples using a 2-part epoxy (detailed below in Section 3.1.3) with a slightly lower viscosity and higher curing time than Dragon Skin 10, which exacerbates settling. We estimated the void content in the resulting specimens by comparing their measured weight against the

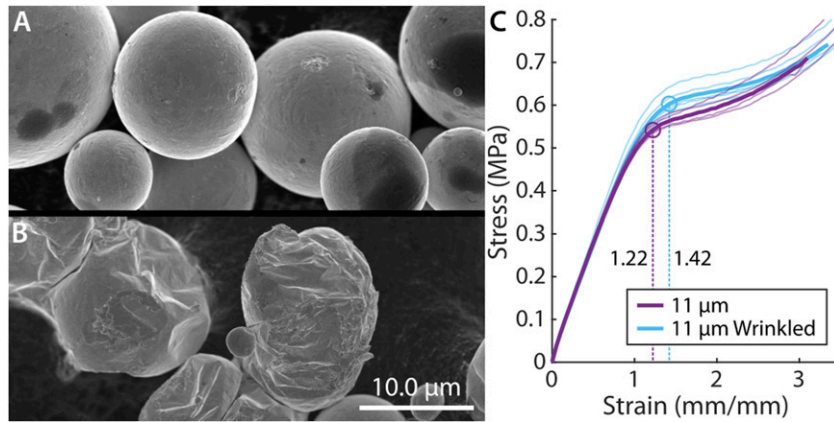


Figure 3. Improved particle bonding via “wrinkling” surface treatment. (a) Neat particles. (b) Particles from the same batch after being heated then quickly submerged in ice water to cause shriveling. (c) Debonding strain is improved by 16%, and debonding stress is improved by 11% over the untreated particles.

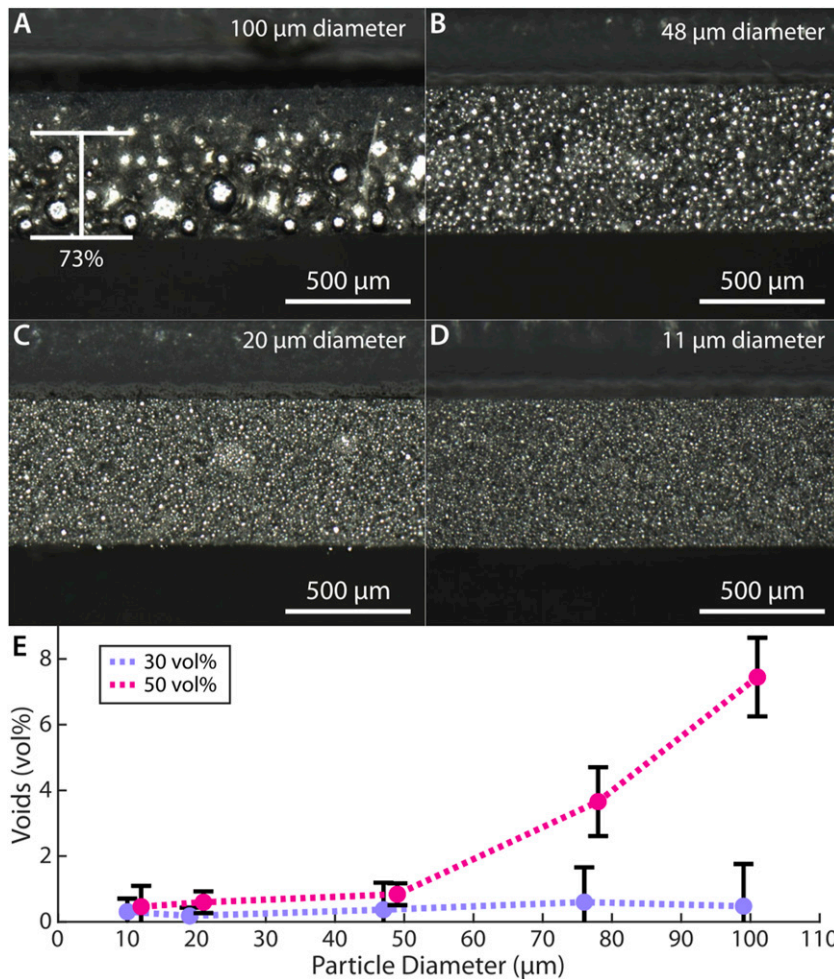


Figure 4. Particle distribution and settling. (a) Composite with a loading of 30 vol% FM in Dragon Skin 10. The largest particle size, mean diameter of 100 μm, settles before the matrix is cured, leaving particles in only the lower 73% of the specimen on average. (b-d) Smaller particles are more evenly distributed throughout the matrix. (e) FM-epoxy composite. At higher loadings, increasing particle diameter causes sedimentation which contributes to the presence of voids.

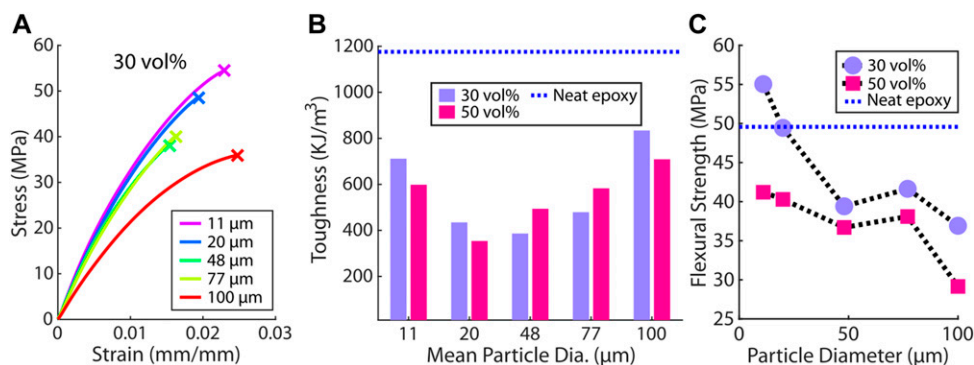


Figure 5. Particle size vs. toughness and strength for FM-Epoxy composites. (A) Representative stress-strain curves of 30 vol% epoxy-FM specimens subjected to 3-point bending until failure. (B) Mean toughness, i.e., energy absorbed per volume before specimen failure as a function of particle diameter. (C) Mean flexural strength as a function of particle diameter.

expected mass for the given specimen volume and FM loading percent, and note a measurable increase in void content as particle size and settling increases, while at 30 vol % the porosity appears approximately uniform regardless of particle size (Figure 4(E)).

Composite strength and toughness. As variable-stiffness structures are often designed to perform move-and-hold operations, the capacity to stiffen in place and subsequently support loads without fracture is especially important. Noting the improved bonding strength of smaller FM particles, we next measured the material toughness and strength. As is well-documented in the literature, the size of additive particles has a significant effect on the durability of the resulting composite. Generally, a reduction in size will result in increased material toughness and increased ultimate strength.^{15,35–37} In addition to the improved bonding characteristics from an increased interfacial surface area, the increased toughness is also usually due to the larger number of rigid particle sites available to arrest crack propagation via deflection or pinning.³⁷

Composite specimens were manufactured from a thermoset epoxy resin consisting of Epon-828 and Jeffamine D-400 combined at the stoichiometric ratio (100:58 by weight), and then loaded with FM particle inclusions at 30 and 50 vol% for a range of particle sizes (5 specimens each). Each specimen, of size $3 \times 10 \times 80$ mm, was subjected to a 3-point-bending test until fracture using a universal testing machine (Instron 3345, Figure 5(A)), with a support span of 48 mm at a loading rate of 2 mm/min.

We calculated the toughness of each specimen by measuring the area under the stress-strain curves, which represents the total energy absorbed by the specimen (KJ/m^3) before failure occurs. In this case, it appears that the largest particles achieve a higher toughness by allowing for larger strains (Figure 5(B)), which may be an artifact of the bilayer system that develops due to settling of the particles as seen in Section 3.1.2, while the smallest particles raise the

toughness via increased flexural strength (Figure 5(C)). Particles of intermediate size suffer from both lower ultimate strength and ultimate strains, and so have the lowest overall toughness. We also note that the more heavily-loaded 50 vol% specimens tended to fracture more easily, which we attribute to the formation of voids within the composite (Figure 4(E)). No specimen could match the toughness of neat epoxy by a factor of almost 1/2, and increasing the filler volume percent increases this disparity by further raising the stiffness and brittleness of the material.

Composite stiffness change and impact of oxide shell. Particle size has significant influence on the composite stiffness change. Part of the undesired stiffening due to smaller particles might be explained by interfacial tension effects, which can cause small liquid inclusions with diameters below a characteristic length scale $D \leq \gamma/E$ to resist deformation, increasing their effective modulus.³⁸ Given the surface tension of liquid Field's metal, $\gamma_{LG} = 417 \text{ mN}/\text{m}$,³⁹ the surface energy of cured epoxy $\gamma_{SG} \approx 35.1 \text{ mN}/\text{m}$,⁴⁰ and the contact angle of Field's metal droplets with our cured epoxy, $\theta = \sim 128^\circ$,¹⁹ we can estimate the interfacial tension between Field's metal and our epoxy $\gamma_{SL} = \gamma_{SG} - \gamma_{LG} \cos(\theta) = 302 \text{ mN}/\text{m}$. Keeping in mind that the oxide shell on the FM can skew these types of interfacial tension measurements,⁴¹ these values along with the modulus of the epoxy matrix material, $E = 11.14 \text{ MPa}$ at 75°C , give a critical diameter of $D = 27 \text{ nm}$. Even using the smallest particle size studied in this work (mean diameter of $11 \mu\text{m}$), our smallest detected particle had a diameter of 371 nm , an order of magnitude larger than the critical diameter (Figure 1(C)) for this particular matrix material.

Instead, we propose that the stiffening behavior in small FM particles is primarily a result of the formation of an oxide shell surrounding each droplet during manufacture, which remains solid while the FM core melts. This oxide shell is mostly composed of In_2O_3 , followed by SnO_2 , and

then Bi_2O_3 ,⁴² all of which are significantly more rigid than Field's metal. Examining a 5 mm × 5 mm planar specimen of Field's metal under X-ray photoelectron spectroscopy (XPS), the presence of Bi_2O_3 was negligible, while we detected SnO_2 at 18 at%, which corresponds to approximately 10.6 wt%. We performed these measurements according to the approach laid out in by Farrell et al⁴³ and Cant et al,⁴⁴ using a magnesium anode, and then again using an aluminum anode which has a higher inelastic mean free path (IMFP) and thus will measure deeper into the oxide. The measurements in both cases are nearly identical, from which we assume that the In_2O_3 and SnO_2 are somewhat mixed, rather than stratified. The mean oxide thickness was measured to be approximately 4.5 nm.

We then estimated the effective modulus of composites containing liquid-core-shell particles following the differential effective medium theory (D-EMT) modified by Garboczi and Berryman,⁴⁵ supplemented with details from Young,⁴⁶ using the material properties in Table 1. This modified model accounts for higher loadings and effects of particle interaction, which is critical for the loading volumes that we explore in this work, and also has a method for converting core-shell particles into an equivalent homogenous particle which allows for analysis of a three-phase composite.

We have collected the resulting equations here for convenience, though we direct the reader to Garboczi and Berryman⁴⁵ for the derivations. First, we define three materials: 1 is the matrix material, 2 is the particle shell material, and 3 is the particle inner core material. ν_i , G_i , K_i , E_i refer to the Poisson's ratio, and the shear, bulk, and elastic moduli of the respective material i . Also, let a and b refer to the diameters of the outer particle shell and of the inner core, respectively. We then calculate the effective properties of the particles $\nu_{\text{eff,p}}$, $G_{\text{eff,p}}$, $K_{\text{eff,p}}$, $E_{\text{eff,p}}$ by replacing the core-shell inclusions with an equivalent homogenous particle of equal size, where $G_{\text{eff,p}}$ is found by solving the following quadratic equation for the positive square root

$$A(G_{\text{eff,p}}/G_2) + 2B(G_{\text{eff,p}}/G_2) + C = 0 \quad (3)$$

with the coefficients given by

$$A = 8z(4 - 5\nu_2)\eta_\alpha p^{(10/3)} - 2(63z\eta_\beta + 2\eta_\alpha\eta_\gamma)p^{(7/3)} \\ + 252z\eta_\beta p^{(5/3)} - 50z(7 - 12\nu_2 + 8\nu_2^2)\eta_\beta p \\ + 4(7 - 10\nu_2)\eta_\beta\eta_\gamma$$

$$B = -2z(1 - 5\nu_2)\eta_\alpha p^{(10/3)} + 2(63z\eta_\beta + 2\eta_\alpha\eta_\gamma)p^{(7/3)} \\ - 252z\eta_\beta p^{(5/3)} + 75z(3 - \nu_2)\eta_\beta\nu_2 p + (3/2)(15\nu_2 - 7)\eta_\beta\eta_\gamma$$

$$C = 4z(5\nu_2 - 7)\eta_\alpha p^{(10/3)} - 2(63z\eta_\beta + 2\eta_\alpha\eta_\gamma)p^{(7/3)} \\ + 252z\eta_\beta p^{(5/3)} + 25z(\nu_2^2 - 7)\eta_\beta p - (7 + 5\nu_2)\eta_\beta\eta_\gamma$$

Table 1. Material properties used in oxide-shell analytical model.

Property	Value	Reference
In_2O_3 with 10 wt% SnO_2		
Young's modulus	116 GPa	[57]
Poisson's Ratio	0.35	[57]
Liquid Field's metal (approximated using liquid indium)		
Bulk modulus	23.96 GPa	[58]
Poisson Ratio	0.5	Estimate
Solid Field's metal		
Young's modulus	9.2 GPa	[19]
Poisson's Ratio	0.33	Estimate
Epoxy @75 °C		
Young's modulus	11.0 MPa	This work
Poisson's Ratio	0.33	Estimate

$$p = (a/b)^3$$

$$z = G_3/G_2 - 1$$

$$\eta_\alpha = z(7 - 10\nu_2)(7 + 5\nu_3) + 105(\nu_3 - \nu_2)$$

$$\eta_\beta = z(7 + 5\nu_3) + 35(1 - \nu_3)$$

$$\eta_\gamma = z(8 - 10\nu_2) + 15(1 - \nu_2) \quad (4)$$

At this point, $K_{\text{eff,p}}$ is found using

$$K_{\text{eff,p}} = K_2 + \frac{p(K_3 - K_2)}{1 + (1 - p)\frac{K_3 - K_2}{K_2 + \frac{4}{3}G_2}} \quad (5)$$

and the remaining values are found using the known relations

$$E_{\text{eff,p}} = \frac{9K_{\text{eff,p}}G_{\text{eff,p}}}{3K_{\text{eff,p}} + G_{\text{eff,p}}}$$

$$\nu_{\text{eff,p}} = \frac{3K_{\text{eff,p}} - 2G_{\text{eff,p}}}{2(3K_{\text{eff,p}} + G_{\text{eff,p}})} \quad (6)$$

As particles are made smaller, the volume percent of oxide material rapidly becomes significant (Figure 6(a)) and begins to stiffen the particles. Although the absolute increase in stiffness appears to be approximately the same whether the particle core is solid or liquid, the relative change in stiffness for liquid-core particles is quite drastic; the predicted modulus of a heated 5 μm particle is $\sim 10\times$ higher than that of a 50 μm particle.

We verified this equivalent particle model by measuring the modulus of individual particles using force spectroscopy via atomic force microscopy (AFM, Asylum Research,

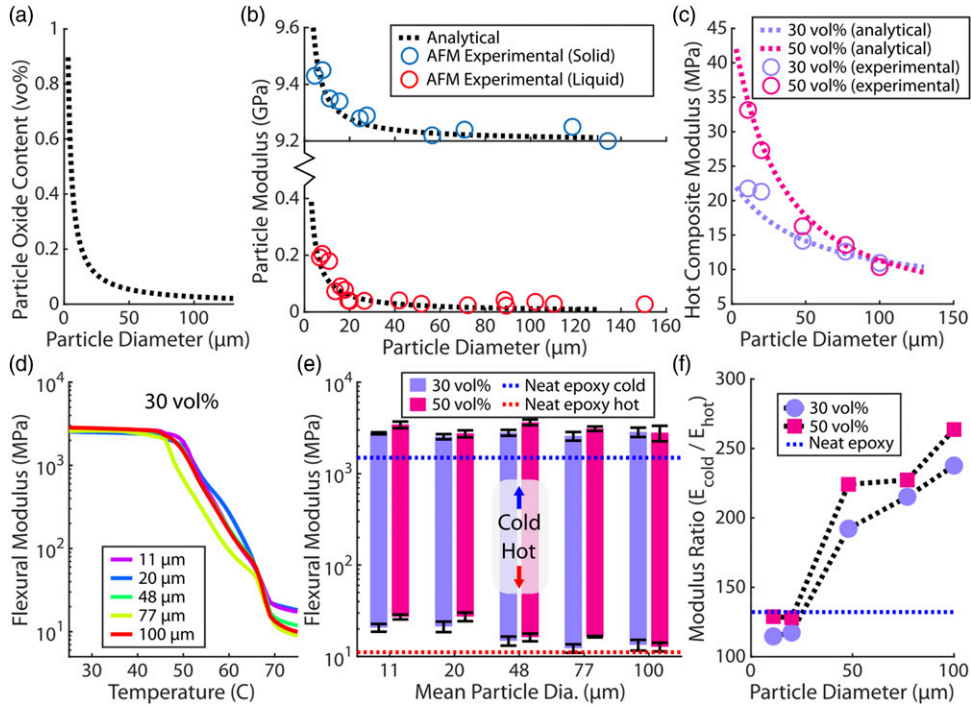


Figure 6. Impact of FM particle oxide shell. (a) The volume percentage of oxide in particles increases sharply as particle size decreases. (b) Elastic modulus of individual FM particles as measured via AFM force spectroscopy. (c) Elastic modulus of FM-epoxy composite at 75°C. The presence of the high-modulus oxide shell impacts the softened modulus and limits the overall stiffness range of the variable-stiffness material. (d) Representative flexural modulus plots of 30 vol% epoxy-FM specimens subjected to temperature sweep. (e) Mean flexural modulus range of each specimen type. The tops of the bars represent the “cold” modulus (25°C), and the bottom is the “hot” modulus (70°C). (f) Mean variable stiffness ratio, $E_{\text{cold}}/E_{\text{hot}}$ for each specimen type.

Cypher ES). While melted, individual particles express some amount of hysteresis, losing some energy to plastic deformation of the particle as the AFM probe tip is pressed into the surface. Hence, we use the force-displacement curve measured during retraction of the tip instead, which exhibits a more nearly elastic response. The AFM probe was moved at a rate of 200 nm/s, indenting to a depth of 20 nm. The probe had a three-sided triangular profile with a rounded tip of radius of ~ 7 nm. During testing, the force curves indeed appeared to follow the response curve of a spherical indenter, which we used as an approximation for the tip shape in the selected Hertz indentation model,⁴⁷ where F is the force response, δ is the cantilever deflection, R is the probe radius, and E and ν are the particle specimen’s Young’s modulus and Poisson’s ratio respectively (1).

$$F = \frac{4}{3} \frac{ER^{1/2}\delta^{3/2}}{(1-\nu^2)} \quad (7)$$

While the Hertz model is not a perfect fit, it sufficiently approximates the value such that we can quantitatively track the overall behavior. The experimental results clearly follow the expected trend from the analytical

plot that small particles suffer from an increased stiffness due to the increased influence of the oxide shell (Figure 6(b)).

We then used the three-phase D-EMT model from Garboczi and Berryman⁴⁵ to predict the modulus of FM particles embedded in the same epoxy medium described in section 3.1.3 (Figure 6(c)). The effective particles resulting from equations (1)–(4) can be used to predict the composite properties G, K

$$\begin{aligned} G &= G_1 / (1 - \phi)^g \\ K &= K_1 / (1 - \phi)^k \\ g &= \frac{5 \left(K_1 + \frac{4}{3} G_1 \right) (G_{\text{eff,p}} - G_1)}{3G_1 \left(K_1 + \frac{8}{9} G_1 \right) + 2G_{\text{eff,p}} (K_1 + 2G_1)} \\ k &= \frac{\left(K_1 + \frac{4}{3} G_1 \right) (K_{\text{eff,p}} - K_1)}{K \left(K_{\text{eff,p}} + \frac{4}{3} G_1 \right)} \end{aligned} \quad (8)$$

and the remaining composite properties E , ν are found as before using the known relations

$$\begin{aligned} E &= \frac{9KG}{3K + G} \\ \nu &= \frac{3K - 2G}{2(3K + G)} \end{aligned} \quad (9)$$

This model was validated by subjecting rectangular epoxy composite specimens of size $3 \times 12.5 \times 30$ mm (5 of each composition) to a thermal sweep from 25°C to 75°C in a 10 mm dual cantilever beam clamp using a Dynamic Mechanical Analyzer (TA Instruments, DMA Q850). Specimens were applied a sinusoidal force on the moving end of cantilever at a rate of 5 Hz, at a strain of 0.02%. Results show an initial drop in flexural modulus between 40 and 50°C, which indicates the onset of glass transition of the epoxy. Up to this point, each specimen exhibits approximately equivalent behavior, as particle size of solid fillers is not expected to significantly affect the composite modulus.^{48,49} For example, at 30 vol%, an initial flexural modulus of ~2.6 GPa at 20°C is reduced to ~60 MPa at 50°C due to the glass transition of the polymer regardless of particle size (Figure 6(d)). However, after the onset of FM particle melting (62°C), it can be seen that decreasing FM particle size has a detrimental effect, reducing the drop in flexural modulus that would be expected from the phase change to liquid (Figures 6(e) and (f)).

Given this behavior, the allowable minimum filler particle size may be limited by the desired lower bound for stiffness change. Alternatively, suppressing the formation of an oxide shell (via acids,⁵⁰ etc.), or use of an entirely different phase-change inclusion material that does not form a shell (such as wax or other polymer) may be a path to mitigating this issue.

Conclusions

By utilizing a thixotropic medium in the manufacture stage, we have shown that it becomes straightforward to repeatedly produce FM particles at a specified size with high sphericity. The approach allows for tuning of variable-stiffness composite properties to a degree that is previously not demonstrated. We also hypothesize that the manufacturing technique presented in Section 2.1 might be useful in other areas. For instance, repeatable control of particle dimensions would benefit the development and optimization of multi-material composites which have previously used low-melting-point metals alongside other fillers, for example to enhance electrical conductivity.^{19,51} We also note that this technique is not limited to metals, and can also be applied to other phase-changing materials such as waxes or thermoplastics.

In seeking a durable variable-stiffness composite, this work shows that dimensional control of the phase-changing inclusions is a key parameter for material performance. In the case of FM, a small particle size can be chosen to enhance bonding between the inclusions and matrix material. This will also increase the composite ultimate strength and toughness. Alternatively, allowing large particles to settle into a densely-packed FM layer reduces the composite strength and stiffness, but can benefit from the natural bilayer formation of neat matrix material above which appears to act as a stabilizing “backbone”, absorbing larger strains before failure. However, matching the toughness of the neat matrix material may require supplemental additives such as rubber nanoparticles⁵² or further bonding enhancements, such as the use of silanes.⁵³

In terms of variable-stiffness, this work suggests that maximizing the modulus range requires larger particle sizes. The presence of a stiff oxide layer becomes a significant impediment to the stiffness-changing ability of the FM particles as particle dimensions are reduced, especially below 50 μm . This impact can be accurately predicted using known analytical models, applicable not only to FM but other oxide-forming materials as well. Increasing the filler content volume also increases the overall stiffness change, although this comes with other downsides, including reduced ease of manufacture and development of voids.

Based on these results, it would seem that for the greatest variable stiffness range of an FM composite, a mean particle size of ~50 μm may be desired, as it does not suffer greatly from the effects of the oxide shell, and can support higher loadings of at least 50% while remaining easily mixable and homogenous without succumbing to large numbers of voids. Much larger particles do not seem to appreciably improve variable-stiffness performance, and risk settling into a layered system at the cost of manufacturing difficulty and high concentrations of voids. Much smaller particles will increase the strength at the cost of reduced variable-stiffness performance, although this may not be an issue for other materials that do not form a shell.

While this work has focused exclusively on the mechanical behaviors of composites with phase-changing particles, there exist other aspects of variable-stiffness to be studied and characterized. Of interest for thermally-responsive phase-changing filler materials are energy costs, heating times, and hotspots, all of which can be reduced by increasing composite thermal conductivity. Thermally-conductive particles such as FM in variable-stiffness composites have already been demonstrated to have a positive impact in this regard,²³ and there is evidence that smaller particles⁵⁵ or a mixture of particle sizes⁵⁶ may be able to improve thermal conductivity further. Electrical conductivity in phase-changing composites is also an area of interest, and studies focused on filler shape⁵⁴ have shown that elongated particles can enable direct Joule heating,

promoting improved integration into systems-level applications. These works, in conjunction with future explorations of different phase-changing filler and matrix materials, all serve to widen and clarify our understanding of the emerging use of inclusions to impart variable-stiffness behavior. As we see phase-changing inclusions becoming more prevalent for variable-stiffness applications, we are optimistic that this work may supply important design considerations and processes for the creation of robust, high-stiffness-change composites.

Declaration of conflicting interests

The author(s) declared no potential conflicts of interest with respect to the research, authorship, and/or publication of this article.

Funding

The author(s) disclosed receipt of the following financial support for the research, authorship, and/or publication of this article: This work was supported by The National Aeronautics and Space Administration (grant no. 80NSSC17K0553).

ORCID iD

Trevor L Buckner  <https://orcid.org/0000-0002-6602-8511>

References

- Hunt LB. The long history of lost wax casting. *Gold Bull* 1980; 13(2): 63–79. DOI: [10.1007/BF03215456](https://doi.org/10.1007/BF03215456).
- Parks A and Yazdani SK. Development of silicone coronary bifurcation models for in vitro flow evaluation. *J Miss Acad Sci* 2014; 59: 383–387.
- McEvoy MA and Correll N. Thermoplastic variable stiffness composites with embedded, networked sensing, actuation, and control. *J Compos Mater* 2015; 49(15): 1799. DOI: [10.1177/0021998314525982](https://doi.org/10.1177/0021998314525982)
- Cheng NG, Gopinath A, Wang L, et al. Thermally Tunable, Self-Healing Composites for Soft Robotic Applications. *Macromol Mater Eng* 2014; 299(11): 1279–1284. DOI: [10.1002/mame.201400017](https://doi.org/10.1002/mame.201400017).
- Shan W, Diller S, Tutcuoglu A, et al. Rigidity-tuning conductive elastomer. *Smart Mater Struct* 2015; 24(6): 065001. DOI: [10.1088/0964-1726/24/6/065001](https://doi.org/10.1088/0964-1726/24/6/065001).
- Wang W, Rodrigue H and Ahn S-H. Smart soft composite actuator with shape retention capability using embedded fusible alloy structures. *Composites B: Eng* 2015; 78: 507–514. DOI: [10.1016/j.compositesb.2015.04.007](https://doi.org/10.1016/j.compositesb.2015.04.007).
- Yoshida S, Morimoto Y, Zheng L, et al. Multipoint Bending and Shape Retention of a Pneumatic Bending Actuator by a Variable Stiffness Endoskeleton. *Soft Robotics* 2018. DOI: [10.1089/soro.2017.0145](https://doi.org/10.1089/soro.2017.0145).
- Zappetti D, Jeong SH, Shintake J, et al. Phase Changing Materials-Based Variable-Stiffness Tensegrity Structures. *Soft Robotics* 2019; 7(3): 362–369. DOI: [10.1089/soro.2019.0091](https://doi.org/10.1089/soro.2019.0091).
- Manti M, Cacucciolo V and Cianchetti M. Stiffening in Soft Robotics: A Review of the State of the Art. *IEEE Robotics Automation Mag* 2016; 23(3): 93–106. DOI: [10.1109/MRA.2016.2582718](https://doi.org/10.1109/MRA.2016.2582718).
- Buckner TL, Yuen MC and Kramer-Bottiglio R. Shape Memory Silicone Using Phase-Changing Inclusions. In: *3rd IEEE International Conference on Soft Robotics (RoboSoft)*, 2020, pp. 259–265. DOI: [10.1109/RoboSoft48309.2020.9116008](https://doi.org/10.1109/RoboSoft48309.2020.9116008).
- Bilodeau RA, Yuen MC and Kramer-Bottiglio R. Addressable, stretchable heating silicone sheets. *Adv Mater Tech* 2019; 4(9): 1900276.
- Bilodeau RA, Nasab AM, Shah DS, et al. Shape Memory Silicone Using Phase-Changing Inclusions Uniform conductivity in stretchable silicones via multiphase inclusions. *Soft Matter* 2020; 16(25): 5827–5839. DOI: [10.1039/D0SM00383B](https://doi.org/10.1039/D0SM00383B).
- Cho J, Joshi MS and Sun CT. Effect of inclusion size on mechanical properties of polymeric composites with micro and nano particles. *Composites Sci Tech* 2006; 66(13): 1941. DOI: [10.1016/j.compscitech.2005.12.028](https://doi.org/10.1016/j.compscitech.2005.12.028).
- Yanase K, Chatterjee H and Ghosh SK. On numerical evaluation of Eshelby tensor for superspherical and super-ellipsoidal inclusions in isotropic elastic material. *Composites Part B: Eng* 2020; 192: 107964. DOI: [10.1016/j.compositesb.2020.107964](https://doi.org/10.1016/j.compositesb.2020.107964).
- Fu S-Y, Feng X-Q, Lauke B, et al. Effects of particle size, particle/matrix interface adhesion and particle loading on mechanical properties of particulate–polymer composites. *Composites Part B: Eng* 2008; 39(6): 933–961. DOI: [10.1016/j.compositesb.2008.01.002](https://doi.org/10.1016/j.compositesb.2008.01.002).
- Kazem N, Hellebrekers T and Majidi C. Soft Multifunctional Composites and Emulsions with Liquid Metals. *Adv Mater* 2017; 29(27): 1605985, DOI: [10.1002/adma.201605985](https://doi.org/10.1002/adma.201605985).
- Chang BS, Mechanically triggered composite stiffness tuning through thermodynamic relaxation (ST3R). *Mater Horiz.*, Jan 2018. DOI: [10.1039/C8MH00032H](https://doi.org/10.1039/C8MH00032H).
- Meerbeek IMV, Morphing Metal and Elastomer Bicontinuous Foams for Reversible Stiffness, Shape Memory, and Self-Healing Soft Machines. *Adv Mater* 2016; 28(14): 2801. DOI: [10.1002/adma.201505991](https://doi.org/10.1002/adma.201505991).
- Buckner TL, Yuen MC, Kim SY, et al. Enhanced Variable Stiffness and Variable Stretchability Enabled by Phase-Changing Particulate Additives. *Adv Funct Mater*; 0(0): 1903368. DOI: [10.1002/adfm.201903368](https://doi.org/10.1002/adfm.201903368).
- Kim SY, Static-state particle fabrication via rapid vitrification of a thixotropic medium. *Nat Commun* 2021; 12(1). DOI: [10.1038/s41467-021-23992-2](https://doi.org/10.1038/s41467-021-23992-2).
- Eristoff S, Kim SY, Sanchez-Botero L, et al. Soft Actuators Made Discrete Grains. *Adv Mater* 2022; 34(16): 2109617. DOI: [10.1002/adma.202109617](https://doi.org/10.1002/adma.202109617).
- Blaiszik BJ, Jones AR, Sottos NR, et al. Microencapsulation of gallium–indium (Ga–In) liquid metal for self-healing

- applications. *J Microencapsulation* 2014; 31(4): 350–354. DOI: [10.3109/02652048.2013.858790](https://doi.org/10.3109/02652048.2013.858790).
23. Buckner TL, Bilodeau RA, Kim SY, et al. Roboticizing fabric by integrating functional fibers. *PNAS* 2020; 117(41): 25360. DOI: [10.1073/pnas.2006211117](https://doi.org/10.1073/pnas.2006211117).
 24. Cutinho J. *Tuning Surface Texture of Liquid Metal Particles by Exploiting Material Metastability*. Graduate Theses and Dissertations, 2017, DOI: [10.31274/etd-180810-5747](https://doi.org/10.31274/etd-180810-5747).
 25. Lauke B. On the effect of particle size on fracture toughness of polymer composites. *Composites Sci Tech* 2008; 68(15): 3365–3372. DOI: [10.1016/j.compscitech.2008.09.011](https://doi.org/10.1016/j.compscitech.2008.09.011)
 26. Nakamura Y, Yamaguchi M, Okubo M, et al. Effect of particle size on the fracture toughness of epoxy resin filled with spherical silica. *Polymer* 1992; 33(16): 3415. DOI: [10.1016/0032-3861\(92\)91099-N](https://doi.org/10.1016/0032-3861(92)91099-N).
 27. Skorina EH. Reverse pneumatic artificial muscles (rPAMs): Modeling, integration, and control. *PLOS ONE* 2018; 13(10): e0204637. DOI: [10.1371/journal.pone.0204637](https://doi.org/10.1371/journal.pone.0204637).
 28. Nicholson DW. On the Detachment of a Rigid Inclusion from an Elastic Matrix. *J Adhes* 1979; 10(3): 255–260. DOI: [10.1080/00218467908544628](https://doi.org/10.1080/00218467908544628).
 29. Valášek P, Müller M and Proshlyakov A. Effect of sedimentation on the final hardness of polymeric particle composites. *Res Agric Eng* 2012; 58(3): 92–98. DOI: [10.17221/5/2011-RAE](https://doi.org/10.17221/5/2011-RAE).
 30. Pukánszky B and Fekete E. Aggregation tendency of particulate fillers: determination and consequences. *Periodica Polytechnica Chem Eng* 1998; 42(2).
 31. Ishai O and Coheno LJ. Effect of Fillers and Voids on Compressive Yield of Epoxy Composites. *J Compos Mater* 1968; 2(3): 302–315. DOI: [10.1177/002199836800200303](https://doi.org/10.1177/002199836800200303).
 32. Schulze KA, Zaman AA and Söderholm K-JM. Effect of filler fraction on strength, viscosity and porosity of experimental compomer materials. *J Dent* 2003; 31(6): 373–382. DOI: [10.1016/s0300-5712\(03\)00091-5](https://doi.org/10.1016/s0300-5712(03)00091-5).
 33. Mysiukiewicz O, Kosmela P, Barczewski M, et al. Mechanical, Thermal and Rheological Properties of Polyethylene-Based Composites Filled with Micrometric Aluminum Powder. *Materials* 2020; 13(5). DOI: [10.3390/ma13051242](https://doi.org/10.3390/ma13051242).
 34. Samal S. Effect of shape and size of filler particle on the aggregation and sedimentation behavior of the polymer composite. *Powder Tech* 2020; 366: 43–51. DOI: [10.1016/j.powtec.2020.02.054](https://doi.org/10.1016/j.powtec.2020.02.054).
 35. Soleymani Shishvan S and Asghari A-H. Particle size effect in metal matrix composites: A study by the continuum theory of stress gradient plasticity, Particle size effect in metal matrix composites: A study by the continuum theory of stress gradient plasticity. *J Compos Mater* 2016; 50(13): 1717–1723. DOI: [10.1177/0021998315595708](https://doi.org/10.1177/0021998315595708).
 36. Karabela MM and Sideridou ID. Synthesis and study of properties of dental resin composites with different nanosilica particles size. *Dental Mater* 2011; 27(8): 825–835. DOI: [10.1016/j.dental.2011.04.008](https://doi.org/10.1016/j.dental.2011.04.008).
 37. Department of Mechanical and Materials Engineering, Faculty of Engineering and Built Environment, Universiti Kebangsaan Malaysia, 43600 UKM Bangi, Selangor, Malaysia et al., “Effects of Filler Size on the Mechanical Properties of Polymer-filled Dental Composites: A Review of Recent Developments,” *JPS*, 29, 141–165, 2018, DOI: [10.21315/jps2018.29.1.10](https://doi.org/10.21315/jps2018.29.1.10)
 38. Style RW, Stiffening solids with liquid inclusions. *Nat Phys* 2015; 11(1): 82–87. DOI: [10.1038/nphys3181](https://doi.org/10.1038/nphys3181).
 39. Zamora R, Martínez-Pastor J and Faura F. Thermal, Viscoelastic and Surface Properties of Oxidized Field’s Metal for Additive Microfabrication. *Materials* 2021; 14(23). DOI: [10.3390/ma14237392](https://doi.org/10.3390/ma14237392).
 40. Page SA, Berg JC and Månson JAE. Characterization of epoxy resin surface energetics. *J Adhes Sci Tech* 2001; 15(2): 153–170. DOI: [10.1163/156856101743382](https://doi.org/10.1163/156856101743382).
 41. Joshipura ID, Are Contact Angle Measurements Useful for Oxide-Coated Liquid Metals? *Langmuir* 1992; 37(37): 2021. DOI: [10.1021/acs.langmuir.1c01173](https://doi.org/10.1021/acs.langmuir.1c01173).
 42. Idrus-Saidi SA, Liquid metal core-shell structures functionalised via mechanical agitation: the example of Field’s metal. *J Mater Chem A* 2019; 7(30): 17876. DOI: [10.1039/C9TA05200C](https://doi.org/10.1039/C9TA05200C)
 43. Farrell ZJ and Tabor C. Control of Gallium Oxide Growth on Liquid Metal Eutectic Gallium/Indium Nanoparticles via Thiolation. *Langmuir* 2018; 34(1): 234–240. DOI: [10.1021/acs.langmuir.7b03384](https://doi.org/10.1021/acs.langmuir.7b03384).
 44. Cant DJH, Wang Y-C, Castner DG, et al. A technique for calculation of shell thicknesses for core-shell-shell nanoparticles from XPS data. *Surf Interf Anal* 2016; 48(5): 274–282. DOI: [10.1002/sia.5923](https://doi.org/10.1002/sia.5923).
 45. Garboczi EJ and Berryman JG. Elastic moduli of a material containing composite inclusions: effective medium theory and finite element computations. *Mech Mater* 2001; 33(8): 455–470. DOI: [10.1016/S0167-6636\(01\)00067-9](https://doi.org/10.1016/S0167-6636(01)00067-9).
 46. Young BA, Effective elastic moduli of core-shell-matrix composites. *Mech Mater* 2016; 92: 94–106. DOI: [10.1016/j.mechmat.2015.09.006](https://doi.org/10.1016/j.mechmat.2015.09.006).
 47. Lin DC, Dimitriadis EK and Horkay F. Robust Strategies for Automated AFM Force Curve Analysis—I. Non-adhesive Indentation of Soft, Inhomogeneous Materials. *J Biomechanical Eng* 2006; 129(3): 430–440. DOI: [10.1115/1.2720924](https://doi.org/10.1115/1.2720924).
 48. Masouras K, Silikas N and Watts DC. Correlation of filler content and elastic properties of resin-composites. *Dental Mater* 2008; 24(7): 932–939. DOI: [10.1016/j.dental.2007.11.007](https://doi.org/10.1016/j.dental.2007.11.007).
 49. Masouras K, Akhtar R, Watts DC, et al. Effect of filler size and shape on local nanoindentation modulus of resin-composites. *J Mater Sci Mater Med* 2008; 19(12): 3561. DOI: [10.1007/s10856-008-3520-4](https://doi.org/10.1007/s10856-008-3520-4).
 50. Mohammed MG, Xenakis A and Dickey MD. Production of Liquid Metal Spheres by Molding. *Metals* 2014; 4(4). DOI: [10.3390/met4040465](https://doi.org/10.3390/met4040465).

51. Nasab AM, Sharifi S, Chen S, et al. Robust Three-Component Elastomer–Particle–Fiber Composites with Tunable Properties for Soft Robotics. *Adv Intell Syst* 2016; n/a, DOI: [10.1002/aisy.202000166](https://doi.org/10.1002/aisy.202000166).
52. Huang F., Effect of Elastomeric Nanoparticles on Toughness and Heat Resistance of Epoxy Resins. *Macromolecular Rapid Commun*; 23(13), 2002, 786–790. DOI: [10.1002/1521-3927\(20020901\)23:13](https://doi.org/10.1002/1521-3927(20020901)23:13).
53. Tee DI., Mariatti M, Azizan A, et al. Effect of silane-based coupling agent on the properties of silver nanoparticles filled epoxy composites. *Composites Sci Tech* 2007; 67(11): 2584–2591. DOI: [10.1016/j.compscitech.2006.12.007](https://doi.org/10.1016/j.compscitech.2006.12.007).
54. Mohammadi Nasab A, Buckner TL, Yang B, et al. Effect of Filler Aspect Ratio on Stiffness and Conductivity in Phase- Changing Particulate Composites. *Adv Mater Tech*; n/a: 2100920. DOI: [10.1002/admt.202100920](https://doi.org/10.1002/admt.202100920).
55. Vo HV, Park DW, Seo WJ, et al. *Effect of Conductive Filler Size and Type on Thermal Properties of Asphalt Mixtures*, 2015, 1–7. DOI: [10.1061/9780784479278.001](https://doi.org/10.1061/9780784479278.001).
56. Li D, Effect of different size complex fillers on thermal conductivity of PA6 thermal composites. *Plastics, Rubber & Composites* 2019; 48(8): 347–355. DOI: [10.1080/14658011.2019.1626596](https://doi.org/10.1080/14658011.2019.1626596).
57. Neerincck DG and Vink TJ. Depth profiling of thin ITO films by grazing incidence X-ray diffraction. *Thin Solid Films* 1996; 278(1): 12–17. DOI: [10.1016/0040-6090\(95\)08117-8](https://doi.org/10.1016/0040-6090(95)08117-8).
58. Li H, Sun Y and Li M. Equation of state of liquid Indium under high pressure. *AIP Adv* 5(9). DOI: [10.1063/1.4931812](https://doi.org/10.1063/1.4931812).